Nano Energy 46 (2018) 29–38

Contents lists available at ScienceDirect

Nano Energy

journal homepage: www.elsevier.com/locate/nanoen

Full paper

Heterostructured nanorod array with piezophototronic and plasmonic effect for photodynamic bacteria killing and wound healing

Xin Yu[a,b,1], Shu Wang[a,c,1], Xiaodi Zhang[a,c], Anhui Qi[a], Xiran Qiao[a], Zhirong Liu[a,c], Mengqi Wu[a,c], Linlin Li[a,c,*], Zhong Lin Wang[a,c,d,*]

[a] Beijing Institute of Nanoenergy and Nanosystems, Chinese Academy of Sciences, Beijing 100083, PR China
[b] Institute for Advanced Interdisciplinary Research, University of Jinan, Jinan 250022, PR China
[c] School of Nanoscience and Technology, University of Chinese Academy of Sciences, Beijing 100049, PR China
[d] School of Materials Science and Engineering, Georgia Institute of Technology, Atlanta, GA 30332-0245, USA

ARTICLE INFO

Keywords:
Bacteria killing
Wound healing
Photodynamic therapy
Piezophototronic effect
Localized surface plasmon resonance (LSPR)

ABSTRACT

Bacteria induced infectious diseases have threated the lives and health of millions people each year. Nanosized titanium dioxide (TiO_2) have been developed for photodynamic bacterial killing with minimal drug resistance, but the efficiency was restricted by their large band gap, limited light-absorption region, and rapid electron-hole recombination. In this work, we rationally fabricated a TiO_2/BTO/Au multilayered coaxial heterostructured nanorod array by inserting a ferroelectric semiconductor barium titanate ($BaTiO_3$) nanolayer between TiO_2 nanorod and gold nanoparticles (AuNPs). The TiO_2/BTO/Au heterostructure showed greatly enhanced reactive oxygen species (ROS) (superoxide ($O_2^{\bullet-}$) and hydroxyl radicals (•OH)) generation, and incident photo-electron conversion efficiency (IPCE) in UV/visible light region. On the basis of experimental observations, the detailed photodynamic mechanism of the enhanced ROS generation was proposed, mainly ascribed to the piezophototronic effect and plasmonic property of the nanorod array. The nanorod array was used as an antibacterial coating to kill gram-negative bacterium *E. coli* and gram-positive bacterium *S. Aureus* with an antibacterial efficiency up to 99.9% under simulated sunlight. It also showed an efficient promotion of infectious wound regeneration in mice with *S. aureus* infected dermal wounds.

1. Introduction

In the past several decades, the abuse of antibiotics for conquering bacteria induced infectious diseases have triggered antibiotic-resistant bacteria, which bring serious problem to human health and eco-environment [1,2]. New alternative antibacterial agents and antibacterial methodologies without antibiotics, *e.g.* photodynamic therapy (PDT), have been developed as a minimally invasive therapeutic modality to conquer multidrug resistance bacteria. PDT takes advantage of photo-induced reactive oxygen species (ROS) generation with photosensitizers, including peroxides (H_2O_2), superoxide ($O_2^{\bullet-}$), hydroxyl radicals (•OH), and singlet oxygen ($^1O_2$) [3]. When used for antibacterial application, the ROS in intimate contact with bacteria would induce the peroxidation of the polyunsaturated phospholipid component of the lipid membrane and promote the disruption of the cell respiration to destroy bacteria [4].

Titanium dioxide (TiO_2) nanomaterials, the most widely used inorganic photocatalyst, could absorb ultraviolet (UV) light to catalyze the ROS generation [5]. Recent researches found that TiO_2 had the highest generation rate of •OH and $^1O_2$ and minimum dark toxicity to avoid harms to normal tissues, compared with inorganic metallic oxide nanoparticles (*e.g.,* ZnO, CeO_2) [6–8]. However, with wide band gap (BG) (3.0–3.2 eV) [9–11], TiO_2 can only absorb and utilize high-energy UV light, which has limited tissue penetration, and also would damage normal tissues at high dose [12]. Moreover, their antibacterial application is remarkably hindered by the limited amount of ROS generation due to the fast recombination of photoexcited electrons (e^-) and holes (h^+) pairs. To overcome these obstacles, noble metal nanoparticles with localized surface plasmon resonance (LSPR) especially gold nanoparticles (Au NPs) have been composited with TiO_2 to form Schottky barrier for the catalytic enhancement [13–15]. The metal nanoparticles can extend the light absorbance from UV to visible region with the assistance of plasmonic effect. Hot-electron injection and plasmon-induced resonance energy transfer are also considered to be main mechanisms for the plasmonic enhancement of photocatalysis [16]. As to the mechanism of hot-electro injection, it is proposed that the

* Corresponding authors at: Beijing Institute of Nanoenergy and Nanosystems, Chinese Academy of Sciences, Beijing 100083, PR China.
E-mail addresses: lilinlin@binn.cac.cn (L. Li), zhong.wang@mse.gatech.edu (Z.L. Wang).
[1] These authors contributed equally to this work.

https://doi.org/10.1016/j.nanoen.2018.01.033
Received 22 December 2017; Received in revised form 12 January 2018; Accepted 19 January 2018

photogenerated hot electrons from Au could be transferred into the conduction band (CB) of neighboring n-type semiconductor, leaving behind holes as the redox centers [17]. However, the energy band alignment of TiO_2 and Au is energetically unfavorable, which unsatisfies the direct transfer of electrons from Au to TiO_2 [18]. Therefore, promotion of the charge separation and transfer to further enhance the photochemical ROS generation is greatly desired for practical antibacterial application.

Piezoelectric and ferroelectric nanomaterials such as ferroelectric $BaTiO_3$ and $LiNbO_3$, multiferroic $BiFeO_3$, and piezoelectric semiconductor ZnO represent a special class of materials with the ability of electrical modulation. These materials have been widely used in the fabrication of photovoltaic and energy harvesting devices [19–21]. Recently, the piezoelectric and ferroelectric property has been used for the promotion of photoinduced electrons-holes separation for photocatalysis *via* building an internal piezoelectric potential [22,23]. With this performance, we hypothesized the rational design of the nanocomposites with a piezoelectric potential may have the ability to promote photodynamic bacterial killing.

In this work, a multilayered coaxial heterostructured nanorod array made with $TiO_2/BaTiO_3/Au$ is successfully synthesized to construct an internal piezoelectric field between TiO_2 and Au. The $BaTiO_3$ nanolayer is deduced to enhance the transportation of the LSPR electrons from Au into TiO_2, which depresses the recombination and promotes the photoinduced PDT. With the enhancement of photoelectrochemical performance, the nanorod array was used as a skin antibacterial coating for photodynamic bacterial killing and infectious skin wound healing *in vitro* and *in vivo*. The nanorod array as an antibacterial coating was able to kill bacterial with an antibacterial efficiency up to 99.9% under simulated sunlight.

2. Results and discussion

Fig. 1a illustrates the preparation process of the multilayered coaxial TiO_2/BTO/Au nanorod array. Firstly, TiO_2 nanorod array was epitaxially gown on a fluorine-doped tin oxide (FTO) substrate *via* a hydrothermal reaction [24]. The outermost layer of the TiO_2 nanorod was subsequently converted to $BaTiO_3$ by *in situ* reaction in the presence of barium precursor through an ion-exchange process. The thickness of $BaTiO_3$ nanolayer could be controlled by tuning the reaction time and barium precursor concentration. Au NPs were then deposited on the TiO_2/BTO core/shell nanorod *via* a physical vapor deposition (PVD) process. For inducing the ferroelectric polarization, a positive polarization (+3 V for 5 min) was exerted to the samples using Pt sheet as the counter electrode in a 2 M KCl electrolyte. The final antibacterial coating has a multilayer TiO_2/BTO/Au coaxial heterostructure on the substrate. The one-dimensional (1D) nanorod array structure with the well-defined exposed crystal facets and high surface area would facilitate the enhancement of light absorption and charge transportation [25].

Fig. 1b–d shows scanning electron microscopy (SEM) images of the top and cross-sectional view of the TiO_2/BTO/Au coaxial heterostructure. Highly aligned nanorods with tetragonal crystallographic planes (*ca.* ~ 2.5 μm in the thickness and 50–150 nm in the nanorod diameter) were observed, and small gold nanoparticles could be discerned (Fig. 1d inset). The high resolution transmission electron microscope (HRTEM) images (Fig. 1e–g) show the surface layer of the TiO_2 nanorod had been successfully converted to tetragonal $BaTiO_3$ (lattice fringe d_{111} = 0.232 nm), distinguishable from interplanar distance of d_{110} = 0.325 nm of rutile TiO_2. The TiO_2/BTO interface was fairly coherent with good lattice match. The $BaTiO_3$ shell thickness was measured to be 5–7 nm, above the critical thickness (~ 2.4 nm) for $BaTiO_3$ to show ferroelectricity at room temperature [26]. A great number of gold nanoparticles (d_{111} = 0.235 nm, face-centered cubic gold) with a mean diameter of about 5 nm were evenly decorated on the surface of the nanorods. Some of the Au NPs had close distance to each other (< 1 nm), which may induce strong local electromagnetic field enhancement *via* the LSPR effect. The multilayered coaxial heterostructure was further proven by element mapping (Fig. 1h), which showed the Au NPs were located at the outmost layer. The positive polarization of TiO_2/BTO/Au with a 3 V voltage had no observable effect on the morphology.

The X-ray diffraction (XRD) results of $TiO_2/BaTiO_3/Au$ showed the peaks from rutile TiO_2, tetragonal $BaTiO_3$ and face-centered cubic Au (Figs. 2a and S4 in the Supporting information). The diffraction peaks located at 26.5°, 33.8°, 37.9°, 51.7°, 61.7°, and 65.8° were indexed to

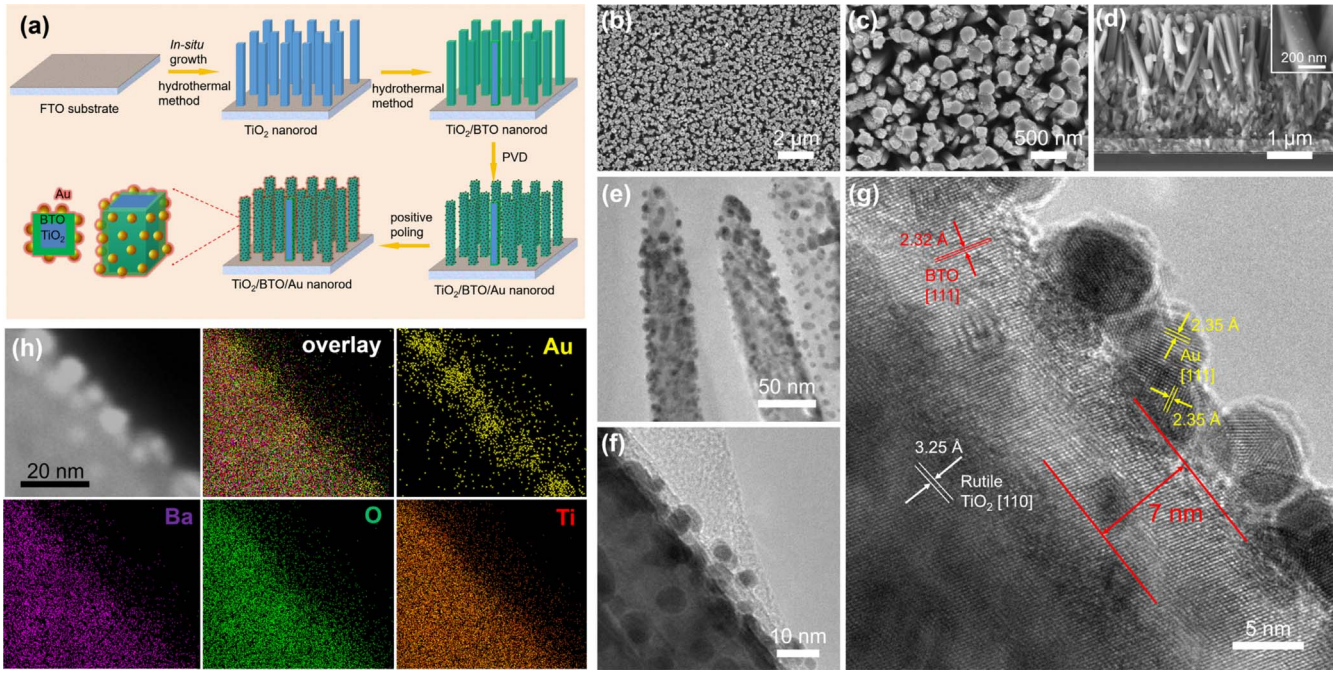

Fig. 1. Fabrication and morphology of TiO_2/BTO/Au nanorod array. (a) Scheme of fabrication process of TiO_2/BTO/Au nanorod array. (b–d) SEM images, (b, c) top surface view, and (d) cross-sectional view of TiO_2/BTO/Au nanorod, (e, f) TEM images and (g) HRTEM image of TiO_2/BTO/Au nanorod, (h) TEM image and EDX element mapping of TiO_2/BTO/Au.

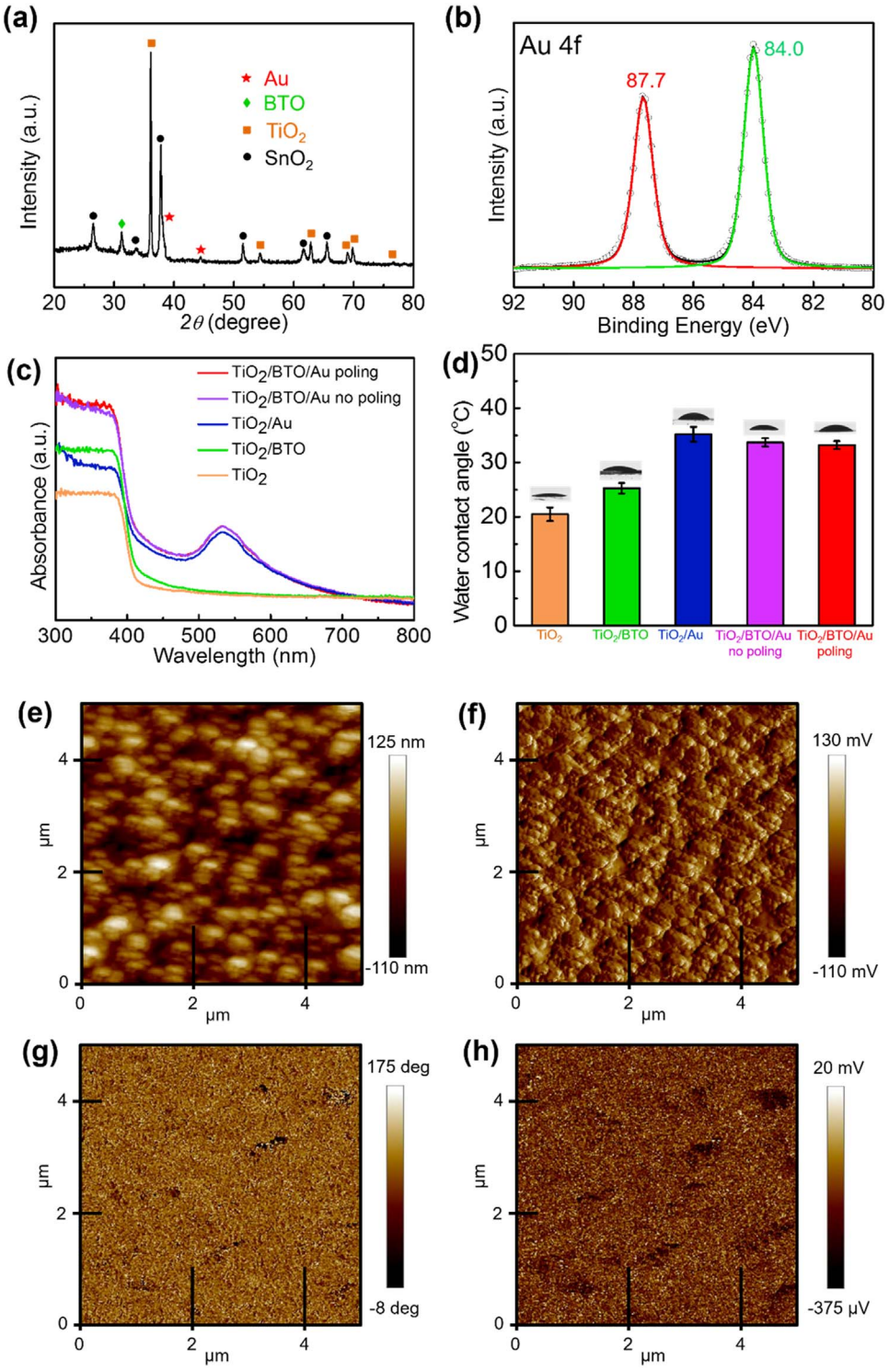

Fig. 2. (a) XRD pattern of TiO_2/BTO/Au on the FTO substrate. (b) XPS characterization of Au 4f for TiO_2/BTO/Au. (c) UV–vis diffuse reflectance spectra and (d) water wettability of TiO_2, TiO_2/BTO, TiO_2/Au, TiO_2/BTO/Au no poling, and TiO_2/BTO/Au with positive poling. (e–f) Piezo-response force microscopy (PFM) images and PFM signals of TiO_2/BTO/Au. (e) AFM surface topography image. PFM images of polarization obtained with voltage = 10 V applied to TiO_2/BTO/Au. (f) Voltage image, (g) phase image and (h) amplitude image.

the (110), (101), (200), (211), (310), and (301) crystal faces of SnO_2 (JCPDS No. 77-0451) of the FTO substrate. The diffraction peaks located at 2θ values of 36.1°, 54.3°, 62.7°, 69.0°, 69.8°, and 76.5° were corresponded to (101), (211), (002), (301), (112), and (201) crystal planes of rutile TiO_2 (JCPDS No. 02-0494) [27]. Peaks belonging to other TiO_2 phases were not detected, indicating the single-crystalline feature of the tetragonal rutile TiO_2 nanorods. The sharp diffraction peaks indicated that the rutile TiO_2 nanorod arrays were highly crystalline. The diffraction peak located at 31.2° was attributed to (101) crystal face of tetragonal $BaTiO_3$ (JCPDS No. 05-0626) [28]. The peaks at 38.2° and 44.4° were assigned to face-centered cube (fcc) Au (JCPDS No. 04-0784) [29]. X-ray photoelectron spectroscopy (XPS) also confirmed the composition and the presence of Ti^{4+} (Ti $2p_{1/2}$ at 464.9 eV and Ti $2p_{1/2}$ at 459.2 eV), Ba^{2+} (Ba $3d_{3/2}$ at 795.2 eV and Ba $3d_{5/2}$ at 780.0 eV), and Au^0 (Au $4f_{7/2}$ at 84.0 eV and Au $4f_{5/2}$ at 87.7 eV) (Figs. 2b and S5 in the Supporting information). UV–visible diffuse reflectance spectra (DRS) showed the TiO_2 nanorod array and TiO_2/BTO core-shell nanorod array had only absorbance in the UV light region. In comparison, TiO_2/BTO/Au heterostructure (with and without positive poling) exhibited remarkably enhanced light absorption with a redshift of band edge to the visible region up to 700 nm (Fig. 2c). An obvious LSPR absorption peak was located at *ca.* 530 nm [30]. These

results indicated that the deposition of Au NPs on TiO_2/BTO could efficiently improve the light utilization especially in the visible light region.

The surface hydrophilicity of an antibacterial coating is an important factor for the biocompatibility [31]. After the fabrication steps for the formation of $BaTiO_3$ and the subsequent Au NPs deposition on the surface of TiO_2 nanorod, the water droplet contact angles (CA, θw) of the sample was continuously increased. It was possibly attributed to the increase of surface roughness of the nanorod array [32]. The samples after each fabrication step still remained hydrophilic wetting characteristic with CA smaller than 35°. For TiO_2/BTO/Au after positive poling, θw was 33.2°. It would facilitate its intimate interaction with bacteria for transporting the generated ROS to bacteria. Typical surface morphology of TiO_2/BTO/Au by atomic force microscope (AFM) was shown in Figs. 2e and S6 (Supporting information), corresponding to that observed by SEM and TEM. Their local piezoelectric characteristics were assessed by measuring the piezoelectric response phase and amplitude under an applied DC bias of piezoresponse force microscopy (PFM). The multilayered nanorod was directly piled with an applied voltage of 10 V to the AFM tip, showing good ferroelectricity (Fig. 2c–f).

For TiO_2 photosensitizer under the UV light illumination, the photogenerated electrons and holes could react with oxygen (O_2) and water (H_2O) to produce $O_2^{\bullet-}$ and $^1O_2$, respectively [33]. $O_2^{\bullet-}$ is not a strong oxidant, which would further react to generate $^1O_2$ and •OH. The reactions are listed in Eqs. (1)–(5).

$$TiO_2 + 2hv \rightarrow TiO_2 + 2h^+ + 2e^- \quad (1)$$

$$2H_2O + 2h^+ \rightarrow 2{\cdot}OH + 2H^+ \quad (2)$$

$$O_2 + e^- \rightarrow O_2^{\cdot-} \quad (3)$$

$$O_2^{\cdot-} + 2H^+ + e^- \rightarrow H_2O_2 \quad (4)$$

$$H_2O_2 + O_2 \rightarrow {}^1O_2 + 2{\cdot}OH \quad (5)$$

To verify the speculation that the insertion of $BaTiO_3$ nanolayer would contribute to the enhancement of ROS generation, the final ROS products of •OH and $^1O_2$ were detected by electron spin resonance (ESR) spectroscopy. 5, 5-dimethyl-1-pyrroline N-oxide (DMPO) and 2, 2, 6, 6-tetramethyl-4-piperidine (TEMP) were used as the spin-trapping adducts of •OH and $^1O_2$, respectively. Fig. 3a showed the signals of DMPO–•OH produced by exposure of the samples to a simulated sunlight (100 mW cm^{-2} for 5 s). For TiO_2/BTO/Au with positive poling ('with poling' was also indicated 'with positive' poling in the following context unless it was specially mentioned), it had the typical hydroxyl radical quad peaks with 1:2:2:1 multiplicity, indicating that the •OH was generated in the photocatalytic process. In comparison, TiO_2/Au and TiO_2/BTO/Au no poling showed weak peaks of DMPO–•OH, whereas the peaks for TiO_2 and TiO_2/BTO with poling were almost indistinguishable. The signal intensity for TiO_2/BTO/Au with poling was over 2.8- folds of those from all the other samples. This result demonstrated that both the loading of Au NPs and the insertion of $BaTiO_3$ nanolayer could increase the •OH generation. The characteristic ESR spectrum of TEMPONE from the reaction of TEMP with captured $^1O_2$ consists of three lines with equal intensities and the hyperfine splitting parameters of the lines are $\alpha_N = 16.0$ [34]. Due to the signal from the hetero-nanostructure and the background signal from the substrate, the half-peak width was widen (Fig. 3b). The signal intensity for TiO_2/BTO/Au with poling was over 4- folds of that from TiO_2, 2- folds of that from TiO_2/BTO and TiO_2/Au, and 1.5- folds of that from TiO_2/BTO/Au without poling, respectively. Thus, TiO_2/BTO/Au with poling under the simulated sunlight illumination had great enhancement of both •OH and $^1O_2$ generation.

To explore the mechanism, the incident photo-electron conversion efficiency (IPCE) spectra were measured to correlate the energy conversion enhancement with the wavelength of the incident light (Fig. 3c and d). At the typical wavelengths from UV to visible region (325–700 nm), TiO_2/BTO/Au with poling had the highest IPCE constantly. For instance, the IPCE at 375 nm was ~50.7%, which was about 2.2- folds of TiO_2, 1.7- folds of TiO_2/BTO with poling, 1.4- fold of TiO_2/Au, and 1.2- folds of TiO_2/BTO/Au no poling, respectively. When the wavelength was moved to the visible light region, the distinction became more obvious. TiO_2 and TiO_2/BTO did not show photo-electron conversion over the wavelength of 400 nm, since TiO_2 and $BaTiO_3$ with wide BG only had light absorption in the UV light region. At 425 nm, the IPCE of TiO_2/BTO/Au with poling (38.5%) was 2.1- folds of TiO_2/Au and 1.5- folds of TiO_2/BTO/Au without poling, respectively. When the wavelength was shifted to 525 nm (close to the LSPR peak of Au NPs), the IPCE of TiO_2/BTO/Au with poling was 4.6- folds TiO_2/Au and 1.8- folds of TiO_2/BTO/Au without poling, respectively. These results demonstrated that both the light absorbance from Au NPs and piezopotential of $BaTiO_3$ played key roles in the increase of photoelectrochemical performance and ROS generation.

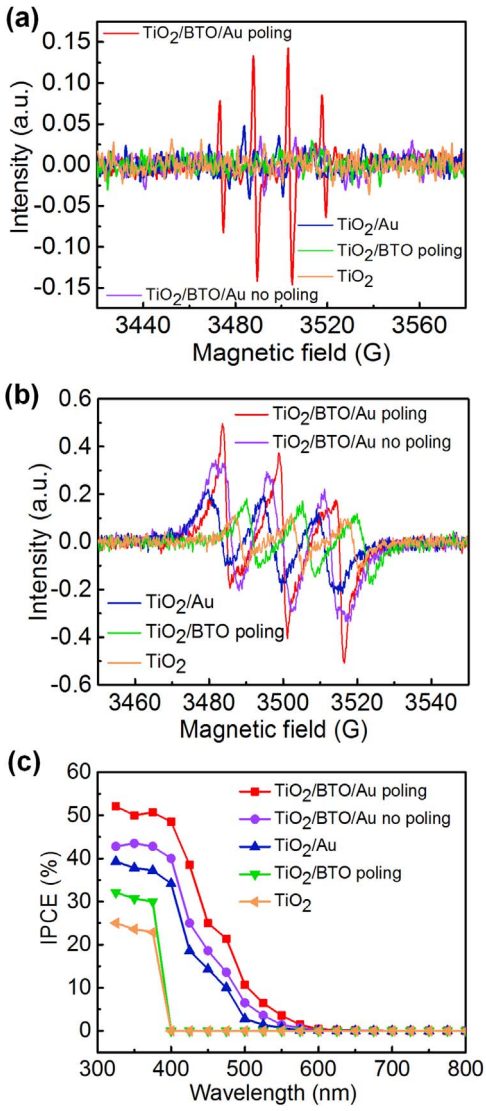

Fig. 3. Measurement of ROS generation and photoelectrochemical performance, and deduced mechanism. ESR spectra of (a) DMPO–•OH with DMPO as the spin-trapping adduct of •OH and (b) TEMPONE with TEMP as the spin-trapping adduct of $^1O_2$. (c) Incident photon-to-current conversion efficiency (IPCE).

According to the above data, the mechanism was deduced as follows (Fig. 4). Tetragonal $BaTiO_3$ is not only a ferroelectric crystal, but also a wide band-gap semiconductor with the BG = 3.20 eV [35,36]. For TiO_2/BTO/Au heterostructure, $BaTiO_3$ formed a heterojunction with

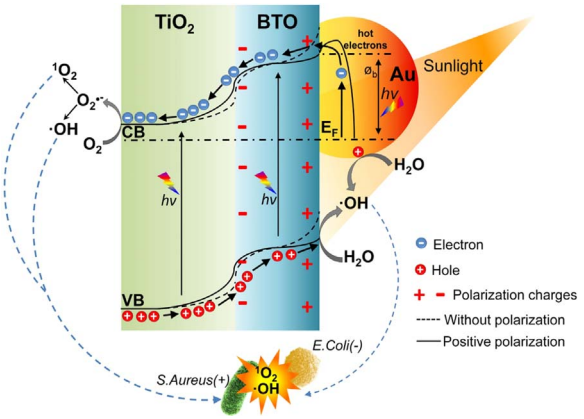

Fig. 4. Mechanism for enhanced photodynamic performance for the TiO_2/BTO/Au heterostructure.

rutile-TiO_2 (BG = 3.0 eV), and typical Schottky junction was built between Au NPs and $BaTiO_3$. Generally, the Schottky barrier may blocks electron transfer from the metal to the semiconductor. Nevertheless, hot electrons generated from the LSPR decay processes of Au NPs had energies higher than the Schottky barrier energy, which could be injected into the adjacent $BaTiO_3$ and facilitated the separation of electron–hole pairs [37]. Under the simulated light illumination, the holes would leave behind and migrate to the Au surface. And hot electrons would migrate inversely from Au to $BaTiO_3$. Under light, both TiO_2 and $BaTiO_3$ could be excited. The generated electrons in $BaTiO_3$ would then migrate to the CB of TiO_2. And the holes in TiO_2 migrate reversely to the valence band (VB) of $BaTiO_3$. More importantly, the piezopotential from ferroelectric semiconductor $BaTiO_3$ could effectively influence the charge transport, resulting in significantly enhanced optoelectronic performances. This is known as the piezophototronic effect in piezoelectric-semiconductor materials [38–41]. Herein, the sample was imposed with a positive polarization, which would form a remnant polarization and a piezopotential between TiO_2 and Au NPs with the positive charges facing Au and the negative charge facing TiO_2. The piezopotential would induce upward band bending and increase the width of the depletion region in TiO_2 and $BaTiO_3$, and reduce the band level of $BaTiO_3$ contacted with Au, simultaneously. It would facilitate the hot-electron transport from Au to $BaTiO_3$, and the photogenerated electrons from $BaTiO_3$ to TiO_2. And simultaneously, it also facilitates the transfer of holes from TiO_2 to $BaTiO_3$ and increases the electron-hole separation. Then, the electrons would react with O_2 in solution to generate $O_2^{\bullet-}$, which would further produce $^1O_2$ and •OH. The holes from the surface of $BaTiO_3$ and Au NPs would react with H_2O to generate •OH. The final products of $^1O_2$ and •OH would further destroy bacteria. Alternatively, if a negative polarization would be exerted on it, there would have a negative effect on the electron and hole transport, the electron-hole pair separation, and the ROS generation [42,43].

So, the whole process is as follows. When the plasmonic Au NPs are in intimate contact with $BaTiO_3$, hot electrons would be excited and

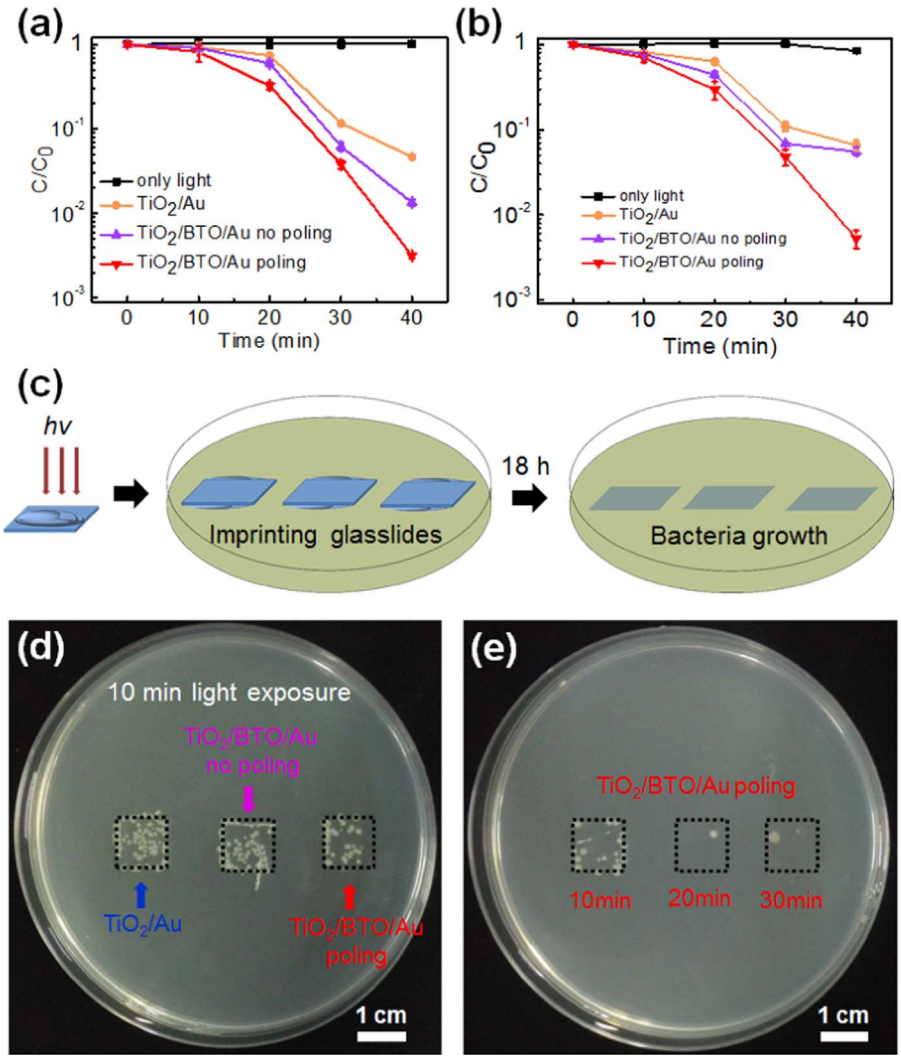

Fig. 5. *In vitro* bacterial killing. Comparison of disinfection performance of the antibacterial coating under simulated sunlight (100 mW cm^{-2}) illumination: (a) *E. coli*, and (b) *S. aureus*. (c) Schematic illustration of a photo-initiated disinfection assay. (d–e) The antibacterial effect for 18 h additional culture after treatment.

transferred from Au NPs to the $BaTiO_3$ nanolayer under the simulated sunlight illumination. Meanwhile, the $BaTiO_3$ nanolayer with ferroelectric polarization would serve as an electron relay, inducing increased charge separation efficiency. Thus, the TiO_2/BTO/Au nanorod array combines both the LSPR of Au NPs and piezophototronic effect of $BaTiO_3$ nanolayer into a single heterostructure to increase the electron-hole separation and the photoactivated ROS generation. The photoactivated ROS would diffuse into the solution and attack the bacteria around, inducing alteration of cell permeability and/or even decomposition of the cell wall [44].

The *in vitro* bacterial killing effect of the antibacterial coating with the multilayered heterostructure was detected by illumination of the bacteria laden coating with the simulated sunlight. A gram-negative bacterium *Escherichia coli* (*E. coli*) and a gram-positive bacterium *Staphylococcus aureus* (*S. aureus*) were used as the representative bacterial models. The antibacterial effect of the different samples are illustrated in Fig. 5a (*E. coli*) and b (*S. aureus*). In the dark condition, the multilayered nanorod array with poling had no antibacterial effect for both *E. coli* and *S. aureus* (Fig. S7 in the Supporting information), demonstrating that it had no dark toxicity. The photoactivated antibacterial activity of $TiO_2/BaTiO_3$/Au with poling was compared with the control samples including 1) bacteria exposed to light alone, 2) bacteria on TiO_2/Au, and 3) bacteria on $TiO_2/BaTiO_3$/Au without poling. Both *E. coli* and *S. Aureus* exposed to light alone for 40 min had the highest cellular survival. For TiO_2/Au and $TiO_2/BaTiO_3$/Au without poling, antibacterial effect was also increased with the light exposure time prolonging from 10 min to 40 min, but the disinfection efficiency was only 93.4% and 94.4% for *E. coli*, the 90.0% and 98.5% for the *S. aureus*. In comparison, the disinfection rate of TiO_2/BTO/Au with poling under 40 min light exposure was > 99.5% for *E. coli* and > 99.7% For *S. aureus*, which was the highest among all the samples. Furthermore, to examine the photocatalytic stability of the catalysts, the efficiency of the photocatalytic antibacterial was assessed by repeating the photocatalysis assessment. As shown in Fig. S9, the *E. coli* and *S. aureus* ware quickly decline of three orders of magnitude after each injection of the *E. coli* and *S. aureus* solution and the photocatalytic antibacterial rate was nearly constant after six repeated experiments.

TiO_2 has distinguished photodriven self-cleaning ability [45]. With this property, we studied the reutilization of the antibacterial coating. The antibacterial activity was assessed by repeating the photoactivated antibacterial assessment with the same sample. As shown in Fig. S9 (Supporting information), the activity of *E. coli* and *S. aureus* was quickly declined for three order of magnitudes after each addition of *E. coli* or *S. aureus*. The photoactivated antibacterial rate was nearly constant after six repeated light-activated antibacterial experiments.

For evaluating the disinfection efficiency of the antibacterial coating, an experiment was used to simulate the tissue surface bacterial killing. The bacterial suspension (*E. coli*; $6*10^4$ CFU mL^{-1}) was dropped onto the heterostructured coatings, followed by a simulated sunlight exposure. The coatings were then imprinted on the nutrient agar plates (simulating the skin tissue surface), followed by an additional incubation of the plates for 18 h at 37 °C to allow the bacteria growth (Fig. 5c). Fig. 5d and e shows the agar plates at the experimental terminal, indicating the bacterial growth as macroscopically visible lawns. With 10 min exposure under the simulated sunlight, there was a robust growth for the bacteria treated with TiO_2/Au and TiO_2/BTO/Au without poling. In contrast, under the same condition, TiO_2/BTO/Au poling led to a significant suppression of bacterial growth. Furthermore, prolonging of the light exposure time from 10 min to 20 and 30 min with TiO_2/BTO/Au poling almost completely prevented the bacterial growth (Fig. 5d and e).

It was worth noting that a 40 min phototreatment with TiO_2/BTO/Au with poling had no effect on the cellular activity of mouse skin fibroblast NIH-3T3. After 40 min light exposure of the cells with TiO_2/BTO/Au poling, the cells had a 92.6% viability compared with that of 95.6% in dark (Fig. 6). It demonstrated that the photoactivated antibacterial process would not harm the normal cells and tissues [46].

In clinic, sunlight has been used in photodynamic therapy of skin diseases [47]. With the favorable *in vitro* antibacterial performance under the simulated sunlight, the multilayered heterostructure was further studied as a dermal antibacterial coating for *in vivo* bacterial killing and wound healing promotion. *S. aureus*, as a common cause of skin infections, was used to construct the wound-infecting skin of mice. Full-thickness dermal wounds on female Balb/c mice were infected with *S. aureus*. After 24 h of successful infection (denoted as 1th day, infection was confirmed by bacterial culture from the wound region), the mice were treated with the antibacterial coating under the simulated sunlight exposure for 30 min (Fig. 7a). The mice in the control group were exposed to the simulated sunlight only. At the 5th day, the wound area in the treatment group was generally smaller than that in the control group. At the 9th day, the wound for most of the mice had vanished in the treatment group and still existed in the control group (Fig. 7b). Wound area of the treatment group decreased faster in contrast to the control group. At the 9th day, the wound closure reached to over 85% for the treatment group, while the control group only reached to less than 70% (Fig. 7c). The body weight of mice reduced after bacterial infection was recovered gradually especially for the treatment group (Fig. S10 in the Supporting information). From hematoxylin and eosin (H&E) staining of the skin tissues from the wounded region, no scar was found for all the mice in the treatment group. Four out of six mice in the treatment group had formed intact epidermis of ~ 200 μm thickness with a seamless interface (Fig. 7d). The neovascularization and regenerated hair follicles could be found. The other two mice after treatment had only slight inflammatory cells in restricted region with the distance < 20 μm (Fig. S11 in the Supporting information). In contrast, 3 out of 6 mice from the control group still had large intersubcutaneous distance (> 100 μm) (Fig. S12 in the Supporting information). For the other 3 mice in the control group, serious interstitial oedema (accumulation of fluid in dermis, arrow 1), parakeratosis (thickness of top-most layer of epidermis, arrow 2), epidermal hyperplasia (arrow 3), and inflammatory infiltration (arrow 4) were observed (Fig. 7e), indicating an incomplete skin healing. Masson's trichrome staining was used to verify the formation of collagen fiber (blue color in Fig. 7f and g) [48]. The dermal tissue in the treatment group showed continuous and arranged collagen fibers in wound location (Fig. 7f), whereas the collagen fibers in the control groups was disorganized and sparse in the inflammatory infiltration region (Fig. 7g). Thus, photoactivated antibacteria with the antibacterial coating can efficiently kill the bacteria, and further promote the wound healing and regeneration.

3. Conclusions

In conclusion, the TiO_2/BTO/Au multilayered coaxial heterostructured nanorod array was successfully synthesized by using a facile process combining the hydrothermal method and PVD method. The integration of piezophototronic effect from $BaTiO_3$ and plasmonic property of Au NPs rendered broad light absorption, high separation efficiency of electron-hole pairs, and ROS generation. The TiO_2/BTO/Au as an antibacterial coating was applied for efficient photodynamic bacteria killing and wound healing *in vitro* and *in vivo*. It would open promising avenues for the designing and fabrication of novel piezoelectric-based heterojunction. We envision that the coaxial heterostructure is also promising candidate for applications in environmental and energy fields.

4. Experimental section

4.1. Materials

All the reagents were analytic grade and commercially available. Titanium tetrachloride ($C_{16}H_{36}O_4Ti$), barium hydroxide ($Ba(OH)_2{\cdot}8H_2O$), diethylene glycol (DEG), ethanol (CH_3CH_2OH),

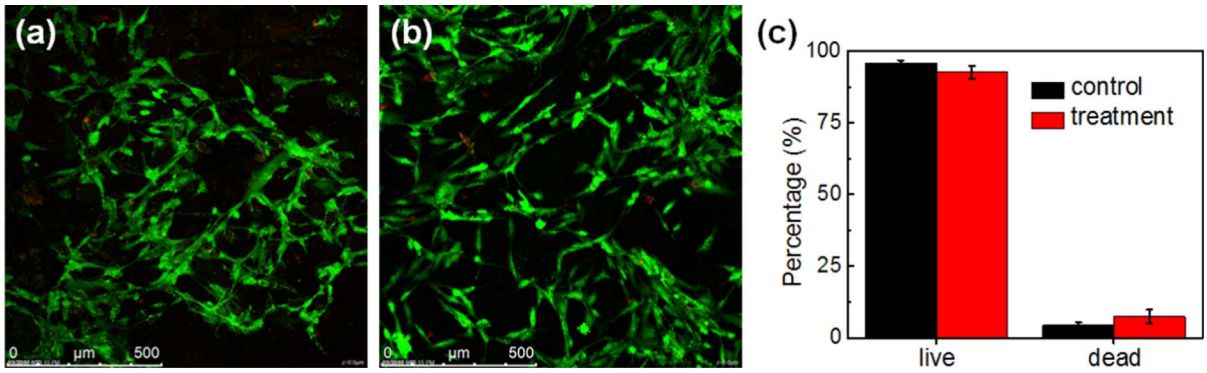

Fig. 6. Effect of photoactivated process on NIH-3T3 fibroblast after (a) exposure under simulated sunlight for *40 min* and (b) in dark. Cells were stained with calcein-AM (green) and EthD-1 (red) to indicate the live and dead cells, respectively. (c) The statistical data showed the percentages of live and dead cells with the assistance of ImageJ software.

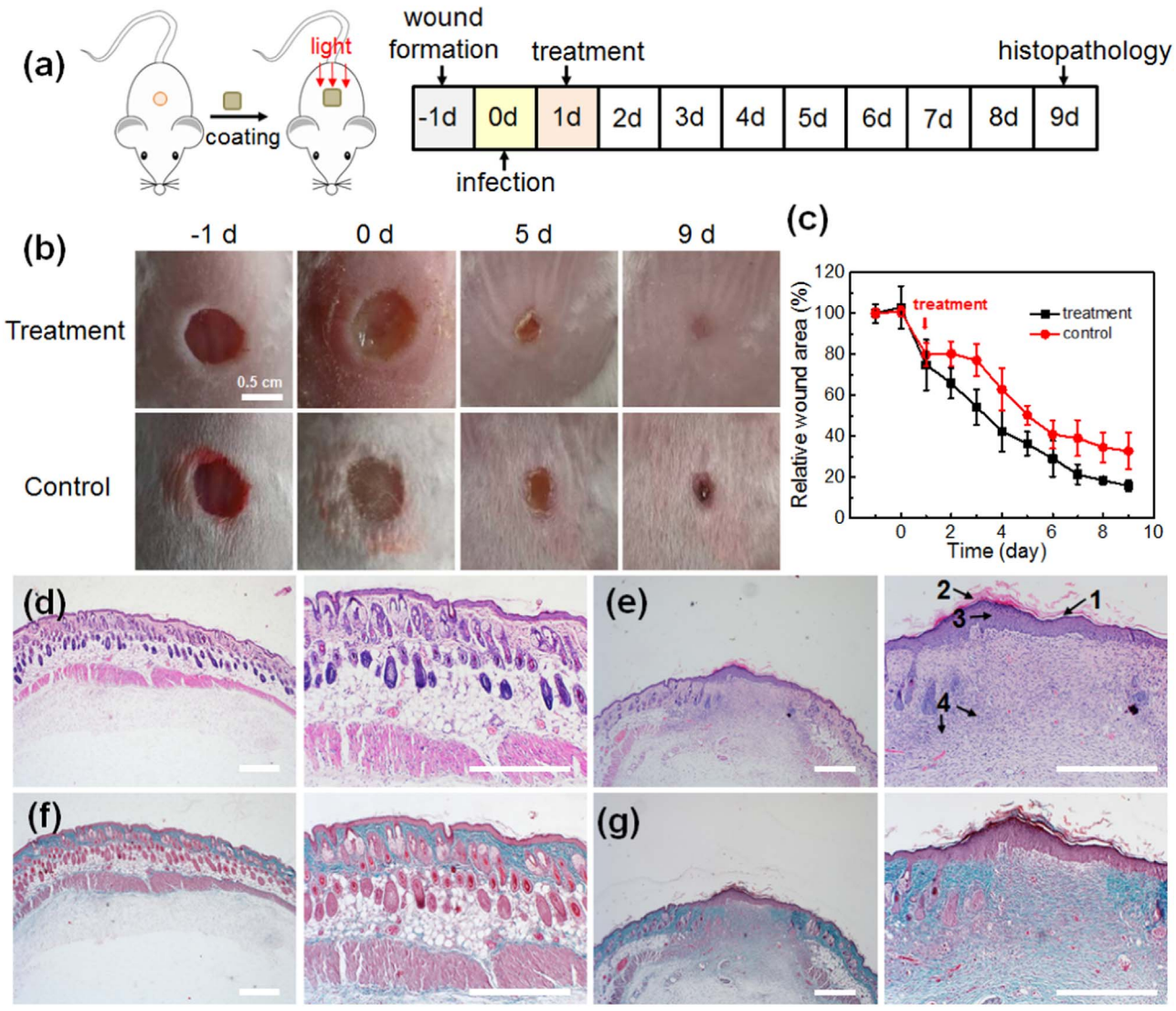

Fig. 7. *In vivo* bacterial killing and skin tissue regeneration in *S. aureus* infected Balb/c epidermal mouse models. (a) Scheme and time schedule of the experiment, (b) representative photographs of wound closure during the nine days *in vivo* treatment. *S. aureus* infected wound was exposed under simulated sunlight for 30 min. (c) Relative wound closure (relative area *versus* initial area). (d–e) H&E staining of tissue sections from (d) the treatment group, and (e) the control group. (f–g) Masson's trichrome staining from (f) the treatment group and (g) the control group. The scale bar in (d–g) is 200 μm.

isopropanol (C_3H_8O) and hydrochloric acid (HCl) were purchased from China National Medicines Corporation Ltd. Tetrabutylammonium hydroxide solution (TBAH, 40 wt%) was purchased from Sigma-Aldrich. All chemicals were used as received without further purification.

4.2. Synthesis of rutile TiO_2 (R-TiO_2) nanorods array

R-TiO_2 nanorod array was prepared on fluorine doped tin oxide (FTO) substrates following our previously reported method.[24] Briefly, a

diluted hydrochloric solution was prepared by mixing 50 mL deionized water with 50 mL hydrochloric acid (6 M), and the mixture was stirred at ambient temperature for 5 min. Then, 500 μL titanium tetrachloride was added to the mixture. The solution was poured into a Teflon-lined stainless steel autoclave. The FTO substrates were ultrasonically cleaned and placed with a 60° angle against the Teflon container wall and the conducting side facing down. The autoclave was sealed and heated to 170 °C for 4 h in an oven. Then, the autoclave was cooled down to room temperature with flowing water. The FTO substrates were rinsed thoroughly with deionized water, and annealed at 500 °C for 2 h in air to improve the crystallinity.

4.3. Synthesis of $TiO_2/BaTiO_3$/Au multilayered coaxial heterostructure

TiO_2/BTO core/shell nanorod array was fabricated by *in situ* converting the surface layer of TiO_2 to $BaTiO_3$ *via* a hydrothermal reaction. Specifically, TiO_2 grown samples were first immersed in a sealed Teflon-lined stainless steel autoclave (50 mL) that filled with a solution of 0.75 mM $Ba(OH)_2{\cdot}8H_2O$ in 5 mL diethylene glycol (DEG), 5 mL ethanol, 1.5 mL isopropanol, 0.6 g tetrabutylammonium hydroxide solution (TBAH, 40 wt%), and 7 mL deionized water. The container was then transferred to the oven and reacted at 170 °C for 4 h. After cooling down to room temperature, the samples were repeatedly washed with deionized water, ethanol, and dried in air in sequence. Au NPs were deposited on surface of the samples with $TiO_2/BaTiO_3$ by magnetron sputtering with a gold target for 30 s (JEOL, JFC-1600). For positive polarization, the TiO_2/BTO/Au nanorod arrays were poled with a +3 V voltage for 5 min in the 2 M KCl aqueous electrolyte using a Pt sheet as the counter electrode.

4.4. Characterizations

XRD patterns were obtained on a Bruker D8 Advance powder X-ray diffractometer with Cu-Kα radiation (λ = 0.15406 nm). The morphology and microstructure of the samples were examined by SEM-a HITACHI S-8020 microscopy. The TEM images were acquired on a FEI/Tecnai G2 F20 S-TWIN TMO microscope with an operating voltage of 200 kV. The UV–visible transmittance spectra of the samples were recorded on a UV–vis spectrophotometer (Shimadzu, UV-3600) with an integrating sphere attachment within the range of 200–800 nm and with $BaSO_4$ as the reflectance standard. All ESR measurements were carried out using a Bruker E500 ESR spectrometer (Billerica, MA) at an ambient temperature.

4.5. Photoelectrochemical (PEC) measurement

The PEC measurements were carried out with the photoelectrochemistry monochromator (Newport, TLS-300X) as the light source using a typical three-electrode electrochemical cell with the samples as the working electrode, Pt sheet as the counter electrode and a saturated calomel electrode (SCE) as the reference electrode. 1 M NaOH solution was used as the electrolytes. During the J-V and V-t scanning, working electrodes were illuminated by a 150 W Xenon lamp coupled with an AM 1.5 global filter with a light intensity of 100 mW cm^{-2}. J-V and V-t curves were recorded using an electrochemical workstation (Gamry Reference 3000). The wavelength-dependent incident photo-electron conversion efficiency (IPCE) was measured with a 250 W Xe lamp with an aligned monochromator (Oriel Cornstone 130 1/8 m). The IPCE was calculated according to the following equation:

$$\mathrm{IPCE} = \frac{1240\ J}{\lambda I_{light}}$$

where J is the measured photocurrent density at 0 V *versus* Ag|AgCl at *a* certain wavelength (λ), and I_{light} is the irradiance intensity at the specific wavelength (λ).

4.6. Antibacterial activity in vitro

Wide-type *E. coli* (ATCC 25922) and *S. aureus* (ATCC 22004) were provided by China General Microbiological Culture Collection Center. The bacteria were used as the models of Gram-negative and Gram-positive bacterium strains, respectively. The bacteria were grown on the standard beef-peptone-yeast (BPY) agar plate, cultured to the log phase, harvested by a centrifugation at 8000 rpm min^{-1}, and then suspended in the saline solution to a concentration of ~ 5×10^4 CFU mL^{-1}. The antibacterial coating were cut into patches with a size of 1 cm × 1 cm, immersed into the bacteria suspension in 24-well plates (1.5 mL), and then exposed to a solar simulator (Newport) calibrated at air mass 1.5 G (100 mW cm^{-2}) as the light source. The bacterial concentration was measured at different times of light exposure using standard spread-plating techniques. Each sample was gradiently diluted and each dilution in triplicate was plated onto the trypticase soy agar culture medium and incubated at 37 °C for 18 h. The experiments for the antibacterial performance were conducted in duplicate. Bacteria survival rate was calculated using the following equation:

$$\%\mathrm{survival} = C/C_0 \times 100\%,$$

where C is the terminal concentration of bacteria and C_0 is the concentration at t = 0 of the experiments.

4.7. In vivo antibacterial activity and wound healing

Balb/c mice (female, 6 weeks, 16–18 g body weight) were obtained from Vital River Corp. Beijing. The animals were kept in an environment complying with the NIH guidelines for the care and use of laboratory animals. All animal procedures were performed following protocol approved by the Institutional Animal Care. The dorsal hair of mice was shaved and the animals were anesthetized by intraperitoneal (i.p.) injection of pentobarbital sodium with a dose of 40 mg kg^{-1} body weight. A rounded full-thickness skin wound (Φ = 6 mm) was created by excising the dorsum of the animals on the backside. The wounds were infected with 10 μL (10^6 CFU mL^{-1}) *S. aureus* and bandaged with elastic bandages. Twenty-four hours later, the wound infection was checked by routine swab culture and treated with photodynamic therapy. Briefly, the excised wounds were covered with the antibacterial coating (1 cm × 1 cm) and exposed to the solar simulator for 30 min (n = 6). For the control group, the animals were only exposed to the solar simulator for 30 min. Then, the animals were individually housed in cages and allowed to heal. The body weight and wound size of the animals were recorded daily. At the termination of the experiments, the animals were sacrificed. The skin tissues of the wound regions were retrieved. The tissues were fixed in 10% formalin, embedded in paraffin, sectioned in 8 μm thick sections, and used for hematoxylin and eosin (H&E) staining and Masson's trichrome staining for histological examination using standard techniques.

4.8. Statistics

The results are expressed as mean ± standard deviation. Standard deviation is indicated by the error bars. Student's *t*-test was used to determine significance among the small groups.

Acknowledgements

The work was supported by the National Natural Science Foundation of China (No. 81471784), the Youth Innovation Promotion Association of the Chinese Academy of Sciences (2015023), Nature Science Foundation of Beijing (2172058), and the "Thousands Talents" program for pioneer researcher and his innovation team, China.

Competing financial interests

The authors declare no competing financial interests.

Appendix A. Supporting information

The supporting information is available free of charge on the Publications website.

Supplementary methods, and additional experimental data (Figs. S1–S13).

Supplementary data associated with this article can be found in the online version at http://dx.doi.org/10.1016/j.nanoen.2018.01.033.

References

[1] K.E. Jones, N.G. Patel, M.A. Levy, A. Storeygard, D. Balk, J.L. Gittleman, P. Daszak, Nature 451 (2008) 990–993.
[2] W.H. Organization, World Health Organization, 2002.
[3] S.S. Lucky, K.C. Soo, Y. Zhang, Chem. Rev. 115 (2015) 1990–2042.
[4] C. Liu, D. Kong, P.-C. Hsu, H. Yuan, H.-W. Lee, Y. Liu, H. Wang, S. Wang, K. Yan, D. Lin, Nat. Nanotechnol. 11 (2016) 1098.
[5] R.Y. Pelgrift, A.J. Friedman, Adv. Drug Deliv. Rev. 65 (2013) 1803–1815.
[6] J. Shi, H.L. Karlsson, K. Johansson, V. Gogvadze, L. Xiao, J. Li, T. Burks, A. Garcia-Bennett, A. Uheida, M. Muhammed, ACS Nano 6 (2012) 1925–1938.
[7] T. Xia, M. Kovochich, M. Liong, L. Mädler, B. Gilbert, H. Shi, J.I. Yeh, J.I. Zink, A.E. Nel, ACS Nano 2 (2008) 2121–2134.
[8] Y. Li, W. Zhang, J. Niu, Y. Chen, ACS Nano 6 (2012) 5164–5173.
[9] X. Yu, L. Wang, J. Zhang, W. Guo, Z. Zhao, Y. Qin, X. Mou, A. Li, H. Liu, J. Mater. Chem. A 3 (2015) 19129–19163.
[10] X. Yu, J. Zhang, Z. Zhao, W. Guo, J. Qiu, X. Mou, A. Li, J.P. Claverie, H. Liu, Nano Energy 16 (2015) 207–217.
[11] X. Yu, X. Han, Z. Zhao, J. Zhang, W. Guo, C. Pan, A. Li, H. Liu, Z.L. Wang, Nano Energy 11 (2015) 19–27.
[12] E.A. Rozhkova, I. Ulasov, B. Lai, N.M. Dimitrijevic, M. Lesniak, T. Rajh, Nano Lett. 9 (2009) 3337–3342.
[13] J. Du, J. Qi, D. Wang, Z. Tang, Energy Environ. Sci. 5 (2012) 6914–6918.
[14] Y. Tian, T. Tatsuma, J. Am. Chem. Soc. 127 (2015) 7632–7637.
[15] I. Lee, J.B. Joo, Y. Yin, F. Zaera, Angew. Chem. Int. Ed. 123 (2011) 10390–10393.
[16] P. Zhang, T. Wang, J. Gong, Adv. Mater. 27 (2015) 5328–5342.
[17] C. Clavero, Nat. Photon. 8 (2014) 95–103.
[18] X. Wang X, C. Liow, A. Bisht, X. Liu, T.C. Sum, X. Chen, S. Li, Adv. Mater. 27 (2015) 2207–2214.
[19] C.R. Bowen, H.A. Kim, P.M. Weaver, S. Dunn, Energy Environ. Sci. 7 (2014) 25–44.
[20] L. Zhao L, Y. Zhang, F. Wang, X. Hu, X. Wang, B. Ma, H. Liu, Z.L. Wang, Y. Sang, Nano Energy 39 (2017) 461–469.
[21] L. Wang, S. Liu, X. Feng, Q. Xu, S. Bai, L. Zhu, L. Chen, Y. Qin, Z.L. Wang, ACS Nano 11 (2017) 4859–4865.
[22] L. Wang, S. Liu, Z. Wang, Y. Zhou, Y. Qin, Z.L. Wang, ACS Nano 10 (2016) 2636–2643.
[23] A. Bhardwaj, N.V. Burbure, A. Gamalski, G.S. Rohrer, Chem. Mater. 22 (2010) 3527–3534.
[24] X. Yu, Z. Zhao, J. Zhang, W. Guo, J. Qiu, D. Li, Z. Li, X. Mou, L. Li, A. Li, Small 12 (2016) 2759–2767.
[25] S. Hoang, P.X. Gao, Adv. Energy Mater. 6 (2016) 1600683.
[26] M. Trieloff, E.K. Jessberger, I. Herrwerth, J. Hopp, C. Fiéni, M. Ghélis, M. Bourot-Denise, P. Pellas, Nature 422 (2003) 502–506.
[27] D.E. Schipper, Z. Zhao, A.P. Leitner, L. Xie, F. Qin, M.K. Alam, S. Chen, D. Wang, Z. Ren, Z. Wang, ACS Nano 11 (2017) 4051–4059.
[28] W. Yang, Y. Yu, M.B. Starr, X. Yin, Z. Li, A. Kvit, S. Wang, P. Zhao, X. Wang, Nano Lett. 15 (2015) 7574–7580.
[29] F.-X. Xiao, Z. Zeng, B. Liu, J. Am. Chem. Soc. 137 (2015) 10735–10744.
[30] J. Zhang, X. Jin, P.I. Morales-Guzman, X. Yu, H. Liu, H. Zhang, L. Razzari, J.P. Claverie, ACS Nano 10 (2016) 4496–4503.
[31] D. Campoccia, L. Montanaro, C.R. Arciola, Biomaterials 34 (2013) 8533–8554.
[32] Z. Lu, W. Zhu, X. Yu, H. Zhang, Y. Li, X. Sun, X. Wang, H. Wang, J. Wang, J. Luo, Adv. Mater. 26 (2014) 2683–2687.
[33] Z. Zhao, J. Tian, Y. Sang, A. Cabot, H. Liu, Adv. Mater. 27 (2015) 2557–2582.
[34] Y. Liu, H. Wu, M. Li, J.-J. Yin, Z. Nie, Nanoscale 6 (2014) 11904–11910.
[35] S. Wemple, Phys. Rev. B2 (1970) 2679.
[36] X. Yu, Z. Zhao, J. Zhang, W. Guo, L. Li, H. Liu, Z.L. Wang, CrystEngComm 19 (2017) 129–136.
[37] C. Wang, D. Astruc, Chem. Soc. Rev. 43 (2014) 7188–7216.
[38] X. Han, W. Du, M. Chen, X. Wang, X. Zhang, X. Li, J. Li, Z. Peng, C. Pan, Z.L. Wang, Adv. Mater. 29 (2017) 1701253.
[39] H. Zou, X. Li, W. Peng, W. Wu, R. Yu, C. Wu, W. Ding, F. Hu, R. Liu, Y. Zi, Adv. Mater. 29 (2017), http://dx.doi.org/10.1002/adma.20170141.
[40] X. Wen, W. Wu, C. Pan, Y. Hu, Q. Yang, Z.L. Wang, Nano Energy 14 (2015) 276–295.
[41] S. Singh, N. Khare, Nano Energy 38 (2017) 335–341.
[42] Z. Wang, D. Cao, L. Wen, R. X, M. Obergfell, Y. Mi, Z. Zhan, N. Nasori, J. Demsar, Y. Lei, Nat. Commun. 7 (2016) 10348.
[43] D. Cao, Z. Wang, Nasori, L. Wen, Y. Mi, Y. Lei, Angew. Chem. Int. Ed. 53 (2014) 11027–11031.
[44] Y.Y. Song, P. Roy, I. Paramasivam, P. Schmuki, Angew. Chem. Int. Ed. 49 (2010) 351–354.
[45] J. Meng, P. Zhang, F. Zhang, H. Liu, J. Fan, X. Liu, G. Yang, L. Jiang, S. Wang, ACS Nano 9 (2015) 9284–9291.
[46] A.E.I. Ghalbzouri, S. Commandeur, M.H. Rietveld, A.A. Mulder, R. Willemze, Biomaterials 30 (2009) 71–78.
[47] S. Wiegell, S. Fabricius, M. Gniadecka, I. Stender, B. Berne, S. Kroon, B. Andersen, C. Mørk, C. Sandberg, K. Ibler, G. Jemec, K. Brocks, P. Philipsen, J. Heydenreich, M. Hadersdal, H. Wulf, Br. J. Dermatol. 166 (2012) 1327–1332.
[48] W. Yin, J. Yu, F. Lv, L. Yan, L.R. Zheng, Z. Gu, Y. Zhao, ACS Nano 10 (2016) 11000–11011.

Dr. Xin Yu received his Ph.D. degree from Beijing Institute of Nanoenergy and Nanosystems, Chinese Academy of Sciences in 2017. Now he is an assistant professor at Institute for Advanced Interdisciplinary Research, University of Jinan. His current research mainly focused on the design and synthesis of nanomaterials and functional crystals and their applications for environment and energy.

Shu Wang received her undergraduate degree from Dezhou University in 2012. Currently she is pursuing her Ph.D. under the supervision of Prof. Linlin Li at Beijing Institute of Nanoenergy and Nanosystems, Chinese Academy of Science. Her research is mainly focused on designing of nanostructured interfaces for guiding stem cells into specific cell linage, researching the biological effect of physical cues, and building nanostructured scaffold for regenerative medicine.

Xiaodi Zhang received her undergraduate degree from Shandong University in 2014, and her major is Materials Science and Engineering, and now she is a graduate student in Beijing Institute of Nanoenergy and Nanosystems, Chinese Academy of Sciences. Her main research interests focus on application of piezoelectric biomaterials in tissue regeneration.

Anhui Qi received her undergraduate degree from Linyi University in 2015, and her major is biotechnology. Now she is a graduate student in Peking Union Medical College. And she is also a joint student at Beijing Institute of Nanoenergy and Nanosystems, Chinese Academy of Sciences. Her research is mainly focused on the application of nanomaterials in cancer theranostics.

Xiran Qiao received his undergraduate degree from Xi'an Polytechnic University in 2015, and his major is dyeing and finishing, and now he is a graduate student in Tianjin Polytechnic University. And he is also a joint student at Beijing Institute of Nanoenergy and Nanosystems, Chinese Academy of Sciences. His research is mainly focused on cancer theranostics.

Zhirong Liu received her undergraduate degree from China University of Geosciences in 2016. Currently she is a graduate student of Prof. LinLin Li at Beijing Institute of Nanoenergy and Nanosystem, Chinese Academy of Science. Her research is mainly focused on functional nanomaterials/nanodevices for biomedical applications.

Mengqi Wu received her undergraduate degree from Henan Polytechnic University in 2017. Currently she is a graduate student of Prof. LinLin Li at Beijing Institute of Nanoenergy and Nanosystem, Chinese Academy of Science. Her research is mainly focused on photodynamic therapy.

Prof. Linlin Li received her M.S. degree in Biochemistry and Molecular Biology from Beijing Normal University in 2005, and Ph.D. degree in Physical Chemistry from Technical Institute of Physics and Chemistry, Chinese Academy of Sciences in 2008. Currently, she is a professor at Beijing Institute of Nanoenergy and Nanosystems, CAS. Her research interests include biomedical application of nanomaterials and nanodevices (nanogenerator and piezotronic device) in cancer theranostics, biosensoring, and tissue regeneration.

Prof. Zhong Lin Wang received his Ph.D. from Arizona State University in physics. He now is the Hightower Chair in Materials Science and Engineering, Regents' Professor, Engineering Distinguished Professor and Director, Center for Nanostructure Characterization, at Georgia Tech. Dr. Wang has made original and innovative contributions to the synthesis, discovery, characterization and understanding of fundamental physical properties of oxide nanobelts and nanowires, as well as applications of nanowires in energy sciences, electronics, optoelectronics and biological science. His discovery and breakthroughs in developing nanogenerators established the principle and technological road map for harvesting mechanical energy from environment and biological systems for powering a personal electronics. His research on selfpowered nanosystems has inspired the worldwide effort in academia and industry for studying energy for micro-nano-systems, which is now a distinct disciplinary in energy research and future sensor networks. He coined and pioneered the field of piezotronics and piezo-phototronics by introducing piezoelectric potential gated charge transport process in fabricating new electronic and optoelectronic devices. Details can be found at: www.nanoscience.gatech.edu.